CARBON 49 (2011) 386–397

available at www.sciencedirect.com

ScienceDirect

journal homepage: www.elsevier.com/locate/carbon

Length dependent foam-like mechanical response of axially indented vertically oriented carbon nanotube arrays

Matthew R. Maschmann [a,b], *Qiuhong Zhang* [a,c], *Feng Du* [d], *Liming Dai* [d], *Jeffery Baur* [a,*]

[a] *Air Force Research Laboratory, Materials and Manufacturing Directorate, AFRL/RX, Wright-Patterson Air Force Base, Ohio 45433, USA*
[b] *Universal Technology Corporation, Dayton, Ohio 45432, USA*
[c] *University of Dayton Research Institute, University of Dayton, Dayton, Ohio 45469, USA*
[d] *Department of Chemical Engineering, Case Western University, Cleveland, Ohio 44106, USA*

ARTICLE INFO

Article history:
Received 20 July 2010
Accepted 15 September 2010
Available online 7 October 2010

ABSTRACT

The axial compressive mechanical response of substrate-supported carbon nanotube (CNT) arrays with heights from 35 to 1200 μm is evaluated using flat punch nanoindentation with indentation depths to 200 μm. The compressive behavior is consistent with that of an open-cell foam material with array height playing a role similar to that of occupation density for traditional foam. Mechanical yielding of all arrays is initiated between 0.03 and 0.12 strain and arises from localized coordinated plastic buckling. For intermediate CNT array heights between 190 and 650 μm, buckle formation is highly periodic, with characteristic wavelengths between 3 and 6 μm. Buckle formation produced substantial force oscillations in both the compressive and lateral directions. The compressive elastic modulus of the arrays is obtained as a continuous function of penetration depth and attains a value between 10 and 20 MPa for all arrays during mechanical yield. A qualitative model based upon concepts of cellular foam geometry is advanced to explain the observed CNT buckling behavior.

© 2010 Elsevier Ltd. All rights reserved.

1. Introduction

Aligned CNT arrays have received significant attention for potential use in applications such as thermal [1–7] and electrical [8–11] interface materials, electrical interconnects [12–14], and composite reinforcement agents [15–17]. Though the mechanical compressive performance of CNTs is expected to contribute significantly to the performance of these applications, relatively little is known about the collective mechanical behavior of CNT arrays and how their morphology may influence mechanical response. Although individual CNTs have demonstrated experimentally measured tensile elastic modulus values on the order of 1 TPa [18,19], experimentally obtained compressive modulus values for vertically aligned CNT arrays are often on the order of 10 MPa – a difference of five orders of magnitude. Because of the inherent waviness and strong van der Waals interactions between neighboring CNTs [20], classical Euler–Bernoulli beam theory alone is insufficient for capturing the complex behavior of the networked interactions present within CNT arrays [21]. Current mechanical models of CNT lack the incorporation of the complexities of CNT morphology, and additional insight into the compressive behavior of these networks is required.

Nanoindentation is a popular means for material property evaluation for thin films and coatings. The method employs high precision instrumentation to monitor force and displacement of an indenter tip during compressive loading and unloading of a sample. Elastic properties are typically obtained from the force–displacement slope (stiffness) during initial withdrawal of the tip, where forces arise due to elastic recovery alone. Discrete evaluations of this type are

* *Corresponding author:* Fax: +1 937 255 9072.
E-mail address: Jeff.Baur@wpafb.af.mil (J. Baur).
0008-6223/$ - see front matter © 2010 Elsevier Ltd. All rights reserved.
doi:10.1016/j.carbon.2010.09.034

Report Documentation Page

Form Approved
OMB No. 0704-0188

Public reporting burden for the collection of information is estimated to average 1 hour per response, including the time for reviewing instructions, searching existing data sources, gathering and maintaining the data needed, and completing and reviewing the collection of information. Send comments regarding this burden estimate or any other aspect of this collection of information, including suggestions for reducing this burden, to Washington Headquarters Services, Directorate for Information Operations and Reports, 1215 Jefferson Davis Highway, Suite 1204, Arlington VA 22202-4302. Respondents should be aware that notwithstanding any other provision of law, no person shall be subject to a penalty for failing to comply with a collection of information if it does not display a currently valid OMB control number.

1. REPORT DATE	2. REPORT TYPE	3. DATES COVERED
2011		**00-00-2011 to 00-00-2011**

4. TITLE AND SUBTITLE	5a. CONTRACT NUMBER
Length dependent foam-like mechanical response of axially indented vertically oriented carbon nanotube arrays	5b. GRANT NUMBER
	5c. PROGRAM ELEMENT NUMBER
6. AUTHOR(S)	5d. PROJECT NUMBER
	5e. TASK NUMBER
	5f. WORK UNIT NUMBER
7. PERFORMING ORGANIZATION NAME(S) AND ADDRESS(ES) **Case Western Reserve University,Department of Chemical Engineering,10900 Euclid Avenue,Cleveland,OH,44106**	8. PERFORMING ORGANIZATION REPORT NUMBER
9. SPONSORING/MONITORING AGENCY NAME(S) AND ADDRESS(ES)	10. SPONSOR/MONITOR'S ACRONYM(S)
	11. SPONSOR/MONITOR'S REPORT NUMBER(S)

12. DISTRIBUTION/AVAILABILITY STATEMENT
Approved for public release; distribution unlimited

13. SUPPLEMENTARY NOTES

14. ABSTRACT

The axial compressive mechanical response of substrate-supported carbon nanotube (CNT) arrays with heights from 35 to 1200 lm is evaluated using flat punch nanoindentation with indentation depths to 200 lm. The compressive behavior is consistent with that of an opencell foam material with array height playing a role similar to that of occupation density for traditional foam. Mechanical yielding of all arrays is initiated between 0.03 and 0.12 strain and arises from localized coordinated plastic buckling. For intermediate CNT array heights between 190 and 650 lm, buckle formation is highly periodic, with characteristic wavelengths between 3 and 6 lm. Buckle formation produced substantial force oscillations in both the compressive and lateral directions. The compressive elastic modulus of the arrays is obtained as a continuous function of penetration depth and attains a value between 10 and 20 MPa for all arrays during mechanical yield. A qualitative model based upon concepts of cellular foam geometry is advanced to explain the observed CNT buckling behavior.

15. SUBJECT TERMS

16. SECURITY CLASSIFICATION OF:			17. LIMITATION OF ABSTRACT	18. NUMBER OF PAGES	19a. NAME OF RESPONSIBLE PERSON
a. REPORT	b. ABSTRACT	c. THIS PAGE			
unclassified	**unclassified**	**unclassified**	**Same as Report (SAR)**	**12**	

considered valid only at the depth of initial tip withdrawal. To evaluate elastic properties as a continuous function of penetration depth, the continuous stiffness measurement (CSM) technique introduces relatively high frequency loading and unloading cycles by imparting a small sinusoidal displacement at the indenter tip superimposed upon the larger steady tip displacement rate. In such a way, stiffness and elastic properties may be evaluated at each data collection interval. Multiple thorough nanoindentation reviews exist in the literature detailing the theoretical basis of the technique, effects of tip geometry, and applications [22–25].

Several researchers have employed nanoindentation and similar instrumented indentation methods as means to evaluate the compressive mechanical properties of CNT arrays [26–34], the results of which are summarized in Table 1. Tested CNT morphologies include short, non-interacting arrays [26,27], typical CVD-grown arrays with heights from 15 μm to over 1 mm [28–33], and densely populated and highly aligned CNT brushes [34]. Data collection techniques and hardware inconsistencies make bridging data sets difficult, and as a result no clear trends may be established relating the mechanical properties to CNT array parameters such as length, diameter, and morphology based upon the available data. Compressive elastic properties within the literature are evaluated most commonly using three techniques. These include evaluations based upon the initial stress–strain loading slope, tangential unloading stiffness, or the CSM technique. Because of the elastic–plastic behavior of most CNT arrays, the loading slope may be significantly lower than that of the unloading slope, directly leading to differences in calculated modulus results. To further confound data, indentation tip geometries vary between experiments and include spherical, pyramidal, Berkovich, rectangular struts, and flat punch geometries. The influence of tip geometry relative to the elastic behavior of CNT arrays is not well studied, though unintended transverse forces will undoubtedly be imparted to the CNT tips utilizing angular tips. Nevertheless, most evaluations report an array elastic compressive modulus of less than 100 MPa. A thorough parametric study of CNT array morphology may help to decouple trends associated with experimental technique from those generated by the CNT arrays themselves.

The mechanical yield of indented CNT arrays, defined as a reduction in the stress–strain slope after initial linear loading, has likewise been observed during indentation [26–29,34]. For those experiments producing yielding behavior, typical buckling yield strains range from 0.01 to 0.6, as observed in Table 1. Others have evaluated only the top several microns of an array, a penetration depth that presumably precedes the onset of yielding [30–33]. Unfortunately, scanning electronic microscope (SEM) evaluation of yielded arrays after indentation is often not reported, and the morphology change of CNTs resulting from the yielding behavior is unclear. Zbib et al. reported micron-scale wrinkles localized at the base of defined CNT pillars arose uniaxial compression [28]. Significant lateral translation at the base of the pillars occurred during compression, and it is unclear how the translation influenced the wrinkle formation. As with the elastic mechanical property evaluation, consistent trends with respect to mechanical yielding from existing literature are not apparent, and the diversity of indentation techniques further confounds the ability to compare results. As a consequence, the physical mechanisms governing the yielding behavior of indented CNT arrays remain poorly understood, and the specific role of CNT array height over several orders of magnitude with respect to mechanical yielding behavior has not been explored.

Freestanding CNT blocks, removed from a native growth substrate, have similarly been examined in uniaxial compression. Reported elastic compressive modulus values vary from 0.9 to 20.8 MPa – a much narrower distribution than those reported by localized indentation of substrate-adhered CNT arrays. Typically, compression of a freestanding CNT block takes place between parallel compression cylinders, resulting in uniaxial compression over the entire cross section of the block, in contrast to the localized compression imparted by nanoindentation. Freestanding CNT blocks may be generated from direct liberation from a native growth substrate [35–37] or from compression molding of loose CNTs from solution into freestanding columns [38]. Directly-liberated films demonstrate remarkable elastic recovery, even after rigorous mechanical cycling. An 860 μm liberated array was shown to recover its full height after 85% compressive strain, with nearly full recovery observed for hundreds of mechanical cycles [35]. After 10,000 compressive cycles of 85% strain amplitude, the array was lost only 20% of its initial height. Gradual height loss within the CNT blocks was attributed to the formation and evolution of highly coordinated parallel buckling folds observed at the bottom of the array and originating after 200 cycles. In a separate experiment, 500,000 cycles of 15% strain amplitude resulted in a height reduction of less than 5% for a 2.2 mm liberated array [36]. Coordinated buckles were also observed after compression of a 3.4 mm liberated CNT block [37]. Although the CNT buckles were on the order of 10 μm in wavelength, their formation was not readily detected within the resulting stress–strain behavior. In contrast, centimeter-scale pillars cast from CNT solutions recovered to only 40% strain after a single loading to 85% strain, with decreased recovery observed at increased cycles [38]. These drastic differences in compressive response illustrate a strong coupling between CNT array morphology that is currently unexplained.

Within this paper, we report the uniaxial nanoindentation of CNT arrays of similar morphology with heights differing by more than an order of magnitude. By utilizing a flat punch nanoindentation tip, hundreds of microns of penetration depth were achievable without imparting unintended lateral forces. Nanoindentation of substrate-adhered CNT arrays to these depths has not been previously reported. The use of the CSM technique allowed for continuous elastic property evaluation throughout the indentation depth. Lateral force measurements were also recorded as a function of penetration depth, yielding a three-dimensional profile of forces arising during indentation. Metrics of interest for the evaluation include compressive forces, lateral forces, elastic stiffness, and changes in CNT morphology observed using SEM analysis. The resulting mechanical response of the arrays is compared to that of open-cell foam, and the resulting deformation modes are described utilizing concepts of cellular materials.

Table 1 – Reported compressive CNT mechanical properties.

Support substrate	Indenter tip/compressive technique	CNT height	CNT diameter	Onset of buckling strain	Elastic compressive modulus	Modulus computation method
Anodic Alumina [24]	2 μm Flat punch	50, 100 nm	25 nm	0.2, 0.6	N/A	N/A
Anodic Alumina [25]	2 μm Flat punch/100 μm diameter sphere/100 nm Berkovich	50, 100 nm	50 nm	0.2, 0.6 flat punch/N/A, 0.4 sphere/0.05–0.08, 0.15 Berkovich	N/A	N/A
Silicon [26]	Berkovich – 1000 nm diameter tip	60 μm	N/A	0.03	14.9 ± 5.7 MPa	Unloading stiffness
Adhered to solid [27]	1 mm Diameter probe	>1 mm	43 nm	0.1	27.6 MPa[a]	Loading stiffness
Silicon [28]	Quartz strut – 2 × 0.5 mm cross section	15, 40, 500 μm	20–30 nm	N/A	0.22–0.25 MPa	Loading stiffness
Polymer [29]	30 μm Flat punch	>600 μm	15 nm	N/A	N/A	N/A
Crystalline [30]	3-Sided pyramid	570–1100 nm	55–104 nm	N/A	0.9–1.23 Tpa	Bending stiffness
Silicon [31]	Berkovich	N/A	N/A	N/A	40–600 MPa	Continuous stiffness
SiC [32]	2, 10, 27 μm Diameter spheres	0.2 and 1.3 μm	1–3 nm	0.08, 0.03, 0.01	18 GPa	Loading stiffness
Freestanding film [33]	Parallel plates	3.4 mm	53 nm	N/A	0.9 MPa[c]/2.2 MPa[d]	Loading stiffness
Freestanding film [34]	Parallel plates	2.2 mm	50 nm	0.01[b]	2.1 MPa[c]/20.8 MPa[d]	Loading stiffness
Freestanding film [35]	Parallel plates	860 μm	40 nm	0.22	12 MPa	Loading stiffness
Freestanding pillar [36]	Parallel plates	>1 cm	N/A	0.15	10–12 MPa	Loading stiffness

[a] Value removes 3% area normalization.
[b] First mechanical cycle.
[c] Measured at initial loading condition.
[d] Measured after plateau region.

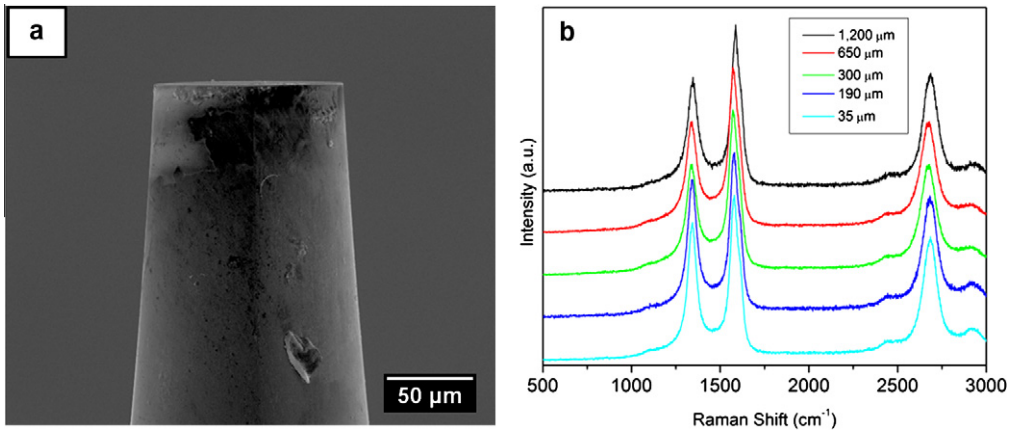

Fig. 1 – (a) SEM micrograph of 100 μm diameter flat punch indenter. (b) Raman spectra obtained from indented CNT arrays. The inset numbers indicate the CNT array heights.

2. Experimental methods

A nominally 100 μm diameter diamond flat punch (Micro Star Technologies) was selected as the nanoindentation tip and is shown in Fig. 1a. The relatively large surface area (9001 μm^2) allows for sensitive detection of the CNT top surface, a nearly uniform contact area with penetration, and uniaxial compression. The flat punch features a taper of less than 5° to a depth of approximately 300 μm from the indenter face. This geometry allows for indentation depths spanning hundreds of microns with little geometrical influence.

Multiwalled CNT arrays were synthesized on 15 × 15 mm SiO_2/Si substrates using two procedures. A 1200 μm array was synthesized utilizing a water-assisted CVD technique incorporating ethylene as a carbon feedstock with hydrogen and helium carrier gasses [39]. This addition of water vapor has been shown to reduce amorphous carbon on catalyst particles, extend catalyst lifetime, and produce CNT arrays in excess of 1 mm [40]. For this procedure a 1 nm thick Fe catalyst layer was deposited atop a 10 nm thick Al_2O_3 buffer film. Water vapor was introduced at concentrations ranging from 200 to 400 ppm. Synthesis proceeded at 1 atm and 760 °C for ten hours to generate an array height of 1200 μm. CNTs produced by this procedure exhibited a diameter distribution between 10–15 nm and 3–8 walls, as observed using transmission electron microscope (TEM) analysis (see Supplementary data). The remaining arrays were produced by utilizing catalyst film with 3 nm Fe atop 10 nm of Al in the absence of water [41]. This procedure yields CNT arrays of various heights depending upon the synthesis conditions. CNT synthesis was achieved at a growth temperature of 750 °C by flowing argon, hydrogen, and acetylene at 10–100 Torr. CNT arrays were synthesized to heights of 35, 190, 300, and 650 μm with this procedure. TEM analysis revealed that CNTs consisted of 2–3 walls (see Supplementary data), with outer diameters between 10 and 20 nm. Raman spectra of the CNT arrays, displayed in Fig. 1b, were obtained by a Renishaw spectrometer operating at a laser wavelength of 532 nm. The ratio of the *D*-band (1340 cm^{-1}) to *G*-band (1580 cm^{-1}) for all samples gives an indication that the arrays were of comparable crystalline quality and composition as measured in the top and off-axis direction with an unpolarized source (see Supporting information). Typical ratios ranged from 0.68 to 0.83, with the 1.2 mm array exhibiting the greatest *D*:*G* ratio.

Instrumented indentation was performed using an MTS Nanoindenter XP system equipped with lateral force and CSM capabilities. The CSM parameters utilized in this study include a 2 nm amplitude and 50 Hz frequency, consistent with recommendations detailed in the MTS machine manual and similar to conditions used by others [34]. Surface contact was defined as the position at which the compressive force–displacement slope exceeded 25 N/m during tip approach. Stress was controlled such that the loading rate divided by the applied load was held at a constant of 0.01 s^{-1}. Such a loading scheme is approximately equivalent to that of a constant indentation strain rate with materials exhibiting constant hardness with depth [42]. A typical duration for a single indent was approximately 3–5 min. Data was collected by indenting no fewer than 20 locations within a given array with grid-like spacing of 200–500 μm between neighboring indents. Spacing between indents had no impact on mechanical response within this separation range. Indents were ceased upon either reaching a maximum displacement of 200 μm for arrays having a height of greater than 300 μm, or upon reaching a defined compressive load of 200 mN for shorter arrays. The indenter tip was cleaned between tests by subjecting the tip to a series of lateral scratch tests on silica, which removed any CNT debris that may adhere to the tip during compression.

3. Results and discussion

To validate the efficacy of the CSM technique with CNT arrays, the elastic stiffness obtained using CSM was compared to that obtained by measuring the tangential unloading stiffness at discrete depths. A 300 μm CNT array was chosen for this evaluation, with 10 locations sampled for each method to a depth of 200 μm. The discrete tangential stiffness measurements from the force unloading curves were obtained at approximately every 20 μm of depth. Stiffness analyses were computed by fitting a linear slope from the beginning of the unloading segment to the point of 40% unloading for both

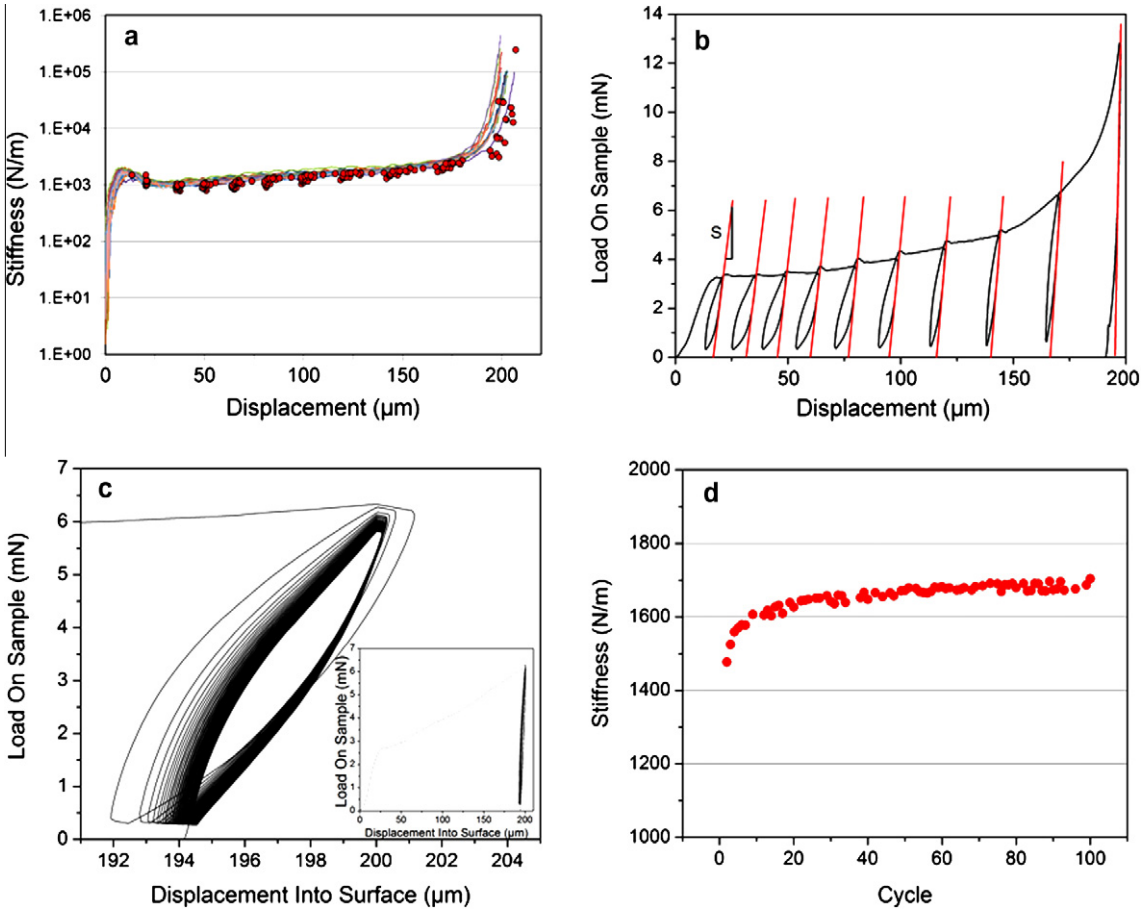

Fig. 2 – (a) Stiffness measured from 300 μm CNT array using CSM (lines) and tangential unloading (filled circles) techniques. (b) Load vs. displacement profile for a typical discrete tangential stiffness measurement. (c) Load–displacement behavior of a 300 μm CNT array for 100 mechanical cycles and (d) the resulting elastic stiffness as a function of mechanical cycle.

methods. Because the unloading slope is not strictly linear, altering the unloading point at which stiffness measurements were calculated resulted in minor changes in measured stiffness values, with the changes remaining relatively consistent between both methods. Prior to alleviation of applied load, the load was held constant for 5 s to minimize potential creep effects. The resulting stiffness profiles are shown in Fig. 2a and show strong agreement with data obtained using the discrete tangential stiffness method. CSM data is displayed as continuous line profiles, while discrete tangential stiffness data are displayed closed circles. Fig. 2b shows significant hysteresis between loading and unloading cycles, consistent with observations of others [43]. Though the CNT arrays recover greater than 1 μm of compression during discrete tangential unloading cycles, compared to less than 2 nm recovery during CSM during stiffness evaluation, a strong agreement exists between the two measurement techniques. As a result, CSM measurements served as the basis for compressive mechanical property evaluation for the remainder of experimental analyses, unless otherwise stated.

To examine the repeatability of elastic stiffness with mechanical cycling, a 300 μm CNT array was loaded to a penetration depth of 200 μm, at which point the load was reduced to 5% of the maximum load. The load was then reapplied until the 200 μm depth was again achieved, and the process was repeated for 100 total cycles. A nearly constant elastic stiffness is maintained with respect to mechanical cycling. Compressive loads were maintained at the maximum and minimum values for 5 s at the end of the unloading and loading cycles to accommodate creep processes. Fig. 2c and d shows the representative mechanical cycling behavior and the resulting tangential unloading stiffness calculated at 40% unload. The hysteresis loop between loading and unloading cycles evolves significantly between first and second cycles, and gradually reaches a repeatable state after approximately 50 cycles. Similar hysteretic behavior has been observed by others [34,38] and has been attributed to energy dissipation from the formation and breaking of neighbor-to-neighbor bonds or viscous loss from air flow induced during compression. Note that the array recovered only 8 μm (4%) of compression after the initial compression cycle, with increasingly less recovery observed at advanced cycles. This corresponds to than 96% retained plastic deformation. As demonstrated in Fig. 2d, the stiffness increases by less than 15% between the first and hundredth cycle, with a repeatable stiffness maintained after approximately 50 cycles. The unloading stiffness evolution is related to the strain recovery behavior in that progressively less strain recovery necessitates an increased stiffness at the point of unloading. After a repeatable strain recovery is established, a constant

stiffness value of approximately 1680 N/m is likewise observed. This behavior demonstrates the potential to tune an array's density and slightly alter the mechanical stiffness.

3.1. *Stress–strain behavior*

Compressive stress is defined as the compressive force divided by the indenter tip face area of 9001 μm^2. The flat punch geometry used in this study simplifies the computation of mechanical stress compared to indenters having spherical or angular geometries, as the cross-sectional area of these types of indenters is a strong function of indentation depth. Similarly, strain was computed by dividing the compressive displacement by the initial CNT array height. These straightforward and intuitive definitions of stress and strain are an additional advantage of utilizing a flat punch tip geometry. Although proper alignment between the face of a flat tip indenter and the sample is a concern, alignment co-planarity differences were measured at less than 1 angular degree. Because of the significant depth of penetration for this study, and in light of potential inherent height variation within the free tip area, any misalignment between the indenter tip and free surface of the arrays is considered to be small and isolated to only the top 2 μm of contact.

The collective compressive response of the arrays, observed in Fig. 3, consists of three distinct stress–strain regions and is consistent with that of an open-cell foam, as was first reported by Cao et al. [35]. The initial region features a linear or near-linear region at low stress, followed by an elongated cellular collapse plateau, and a final densification region in which stress rapidly increases. The plateau region for traditional foam may consist of recoverable elastic buckling, plastic yielding, or brittle crushing, depending on the foam composition and mechanical properties of the cellular strut material. All three mechanisms result in a similar stress–strain behavior. Mechanical behavior in each region is dictated in large part by the relative density of the strut constituent material. The relative density of cellular strut material is strongly related to the thickness and geometry of the struts by the following relationship

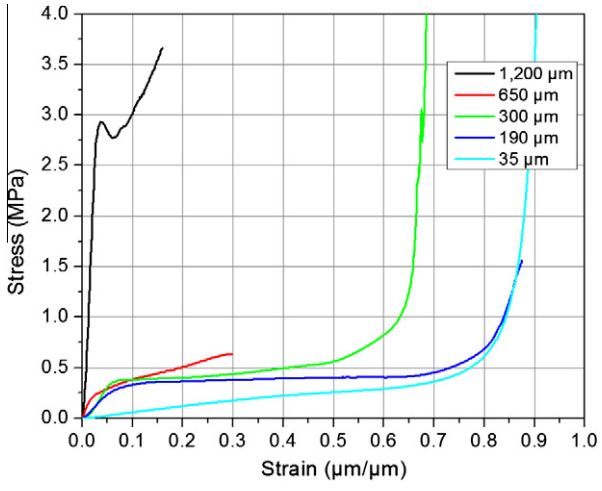

Fig. 3 – Average stress–strain behavior of the indented CNT arrays. The inset numbers indicate the CNT array heights.

$$\frac{\rho^*}{\rho_s} \approx \left(\frac{t}{\bar{l}}\right)^2 \quad (1)$$

where ρ is the mass density, t is the open cell strut thickness, l is the characteristic length of a strut in the direction normal to length, the subscript s refers to the properties of the strut solid material, and the superscript ρ^* refers to the observed properties of the foam material. Proportionality may be determined from the cellular geometry.

The onset of elastic and plastic yield of cellular solids are strongly dependent on relative density and follow the relations

$$\frac{\sigma^*_{el}}{E_s} = C_1\left(\frac{\rho^*}{\rho_s}\right)^2 \quad (2)$$

for elastic foam material and

$$\frac{\sigma^*_p}{\sigma_{ys}} = C_2\left(\frac{\rho^*}{\rho_s}\right)^{3/2} \quad (3)$$

for plastically yielding foam, where σ^*_{el} is the elastic collapse stress, E is the elastic modulus, σ^*_p represents the plastic collapse stress, σ_{ys} is the yield strength of the cellular strut material, and C_1 and C_2 are constants. For low density elastic foam ($\frac{\rho^*}{\rho_s} < 0/3$), a constant of proportionality (C_1) of 0.05 empirically fits most materials. Similarly, the predicted collapse strain for elastic foam is simply equal to the constant of proportionality of 0.05. A value of 0.03 has been experimentally determined for C_2, resulting in a predicted plastic collapse strain similar to that of elastic foam at moderate densities and slightly higher for lower density plastic foam. Similarly, the onset of densification strain in an open-cell foam decreases as a function of relative density.

The average compressive behavior of CNT arrays having various heights, displayed in Fig. 3, is consistent with that of an open-cell foam material of various relative densities. The 35 μm array behaves similarly to low density foam, while the 1200 μm array exhibits the behavior of higher density foam. Intermediate array heights also follow the general relationship that greater CNT heights exhibit behavior of increased foam density. The average yield stress ranges from approximately 0.01 MPa for the 35 μm array to 2.9 MPa for the 1200 μm array. Yield strain occurs at approximately 0.03 for the 1200 μm array to 0.12 for the 35 μm array, with a trend similar to that anticipated for plastically yielding foam [44]. The onset of densification strain decreases with array height, consistent with open-cell foam behavior at various densities.

Closer examination of individual stress–strain curves, shown in Fig. 4, yields additional insight into the compressive behavior of each array and demonstrates the run-to-run variability observed for each sample. The 35 μm array exhibited the greatest run-to-run variability with respect to the yield strain and densification strain, perhaps due in part to difficulty associated with accurate force-based detection of the array surface. It is noteworthy to emphasize that the 35 μm array demonstrated significantly lower initial loading slope relative to the other arrays. Interestingly, all samples other than the 35 μm array exhibit a periodic stress–strain oscillation signature within the plateau region with characteristic wavelengths between approximately 3–6 μm. To investigate the physical mechanism giving rise to the stress–strain oscillations, each CNT array was indented along a free edge of the

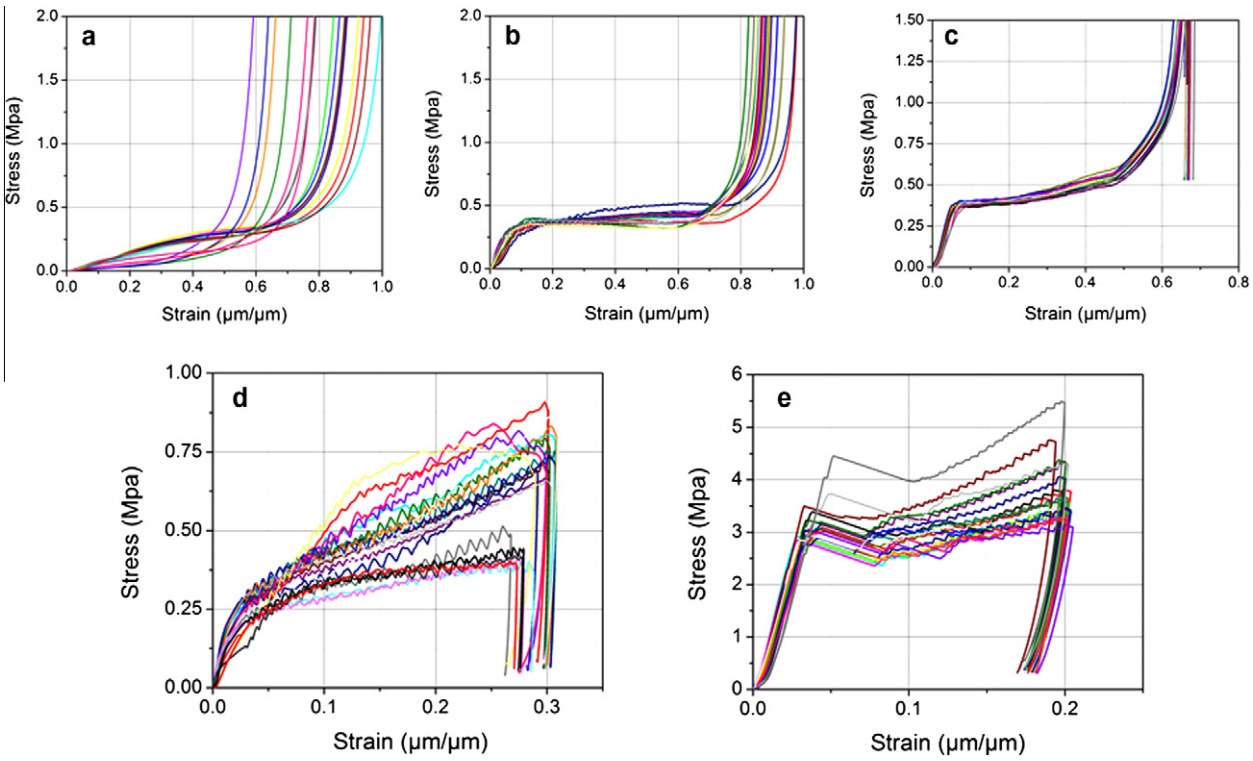

Fig. 4 – Stress–strain relationship for indented (a) 35 μm, (b) 190 μm, (c) 300 μm, (d) 650 μm, and (e) 1200 μm arrays.

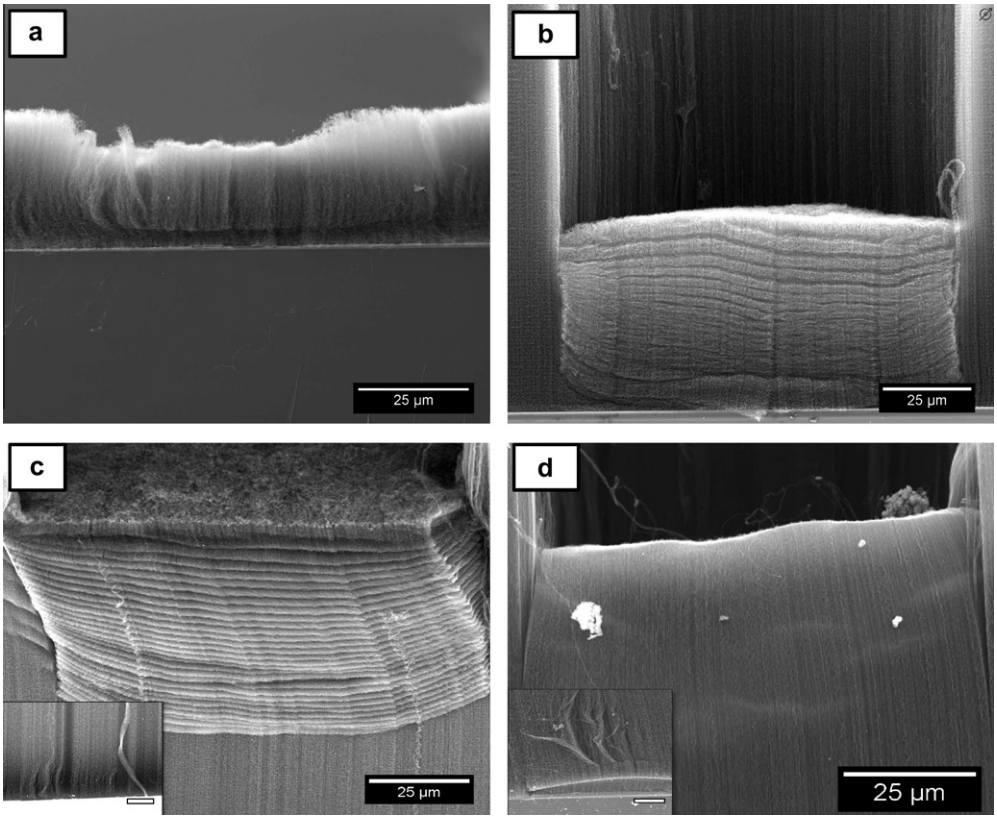

Fig. 5 – Characteristic buckling behavior of (a) 35 μm, (b) 190 μm, (c) 650 μm, and (d) 1200 μm CNT arrays. Scale bars of inset images = 10 μm.

substrate support to a depth exceeding the onset of the yield strain. The stress–strain behavior at the free edges of the samples is consistent with that obtained within the bulk of the sample. This elicits confidence that the observed yielding

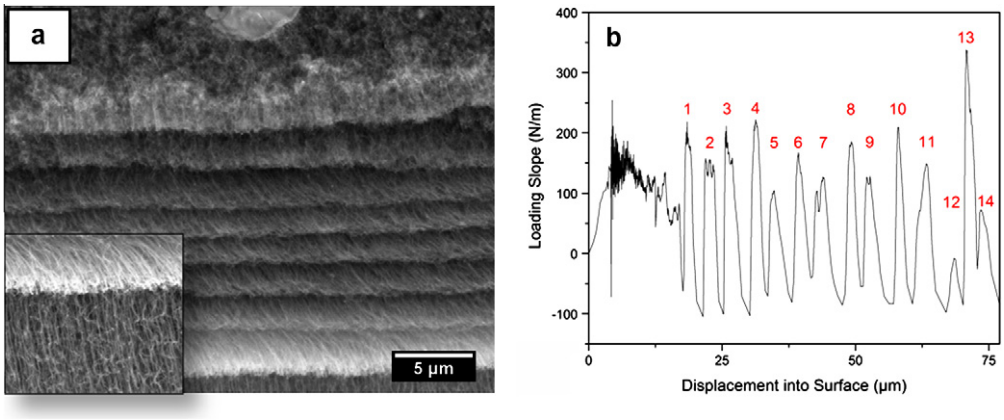

Fig. 6 – Buckling characteristics of 650 μm CNT array. (a) SEM micrograph of buckled region of 75 μm indent with inset showing undisturbed CNTs directly under buckling front. (b) Corresponding instantaneous loading slope for 75 μm indent.

behavior is an intrinsic characteristic of the CNTs, independent from neighboring interactions. Fig. 5 shows cross-sectional SEM images of the indented edges which reveal clear evidence of plastic hinge and buckle formation for each array, consistent with plastic yielding of cellular struts within a foam material.

The 35 μm array displayed an out of plane, S-shaped bending behavior over the height of the array. The buckle is presumed to originate during the plateau region of the stress–strain curve. Arrays having heights of 190, 300, and 650 μm display a different behavior, with similar characteristics. These arrays exhibited localized, accordion-like collective buckling and folding originating at the top surface of the indented array. Increasing indentation depths resulted in the formation of a greater number of buckling folds. No evidence of compression existed within the array region directly beneath the buckling front for these arrays, indicating highly localized compression within the buckling region. However, evidence of a single buckle at the bottom of the array, near the growth substrate, was observed after indentation of the 650 μm array. The bottom buckle is unique in appearance compared to the buckles appearing near the top surface and appears to have recovered a significant portion of deflection. The origination of coordinated buckles near the arrays' top surfaces contradicts results obtained from the compression of liberated millimeter-length CNT arrays, in which coordinated buckling folds were observed strictly on the bottom side of the CNT film [35,37]. Additionally, the deformation observed herein by nanoindentation is largely plastic in nature, with less than 5% strain recovery achieved within the plateau region after one cycle, while uniaxial compression of liberated arrays is largely elastic in nature [35]. Furthermore, SEM examination of the 1200 μm array reveals clearly plastic deformation, with much of the indent strain unrecovered. Despite the occurrence of periodic stress–strain oscillations during indentation, the buckling behavior lacks the organization and coordination exhibited by other arrays. However, isolated small-amplitude ripples spanning a portion of the projected indent area are observed at various depths beneath the surface. A lack of large-scale buckling with largely plastic deformation may indicate densification of CNTs throughout a greater depth of the array. Indeed, Fig. 5d shows that small-scale buckles are not localized at the top of the indented surface, as is the case with other arrays. An additional large wavelength buckle is observed at the bottom of the array (directly above the substrate surface). The observed buckle is similar to that observed after indentation of the 650 μm array, but larger in wavelength. In the absence of *in situ* observation, it is difficult to determine how buckling, densification, and deformation evolved within this array. However, the compressive behavior of this array is unique amongst the others tested and may originate in part from the differentiated synthesis method and differences in wall count. Lower magnification images of the 650 and 1200 μm indented arrays may be found in Supplementary data section.

To demonstrate the relationship between the force–displacement oscillations and the formation of mechanical buckles, the number of stress–strain oscillations was compared to the number of observed mechanical folds. For this examination, the 650 μm array was indented to a depth of 75 μm (0.12 strain) along a free edge of the sample using standard parameters. SEM analysis, shown in Fig. 6, displays seven visible folds after indentation (the top region above the first trough shows no signs of having buckled). To more clearly analyze the number of force oscillations recorded during the nanoindentation, the instantaneous loading slope, displayed in Fig. 6b, was evaluated to magnify the amplitude of oscillations over that observed by force–displacement. The plot reveals 14 force oscillations, corresponding to double the number of folds observed by SEM analysis. Based on this information, we surmise that a complimentary set of buckles exists on the side opposite the free edge observed in Fig. 6a, with each complimentary buckle exhibiting a fold out of phase with those visible at the free edge to form an "S-shaped" fold.

The formation of buckles within the stress collapse plateau is conceptually akin to the formation of plastic hinges exhibited within the cells of traditional open-cell foam undergoing plastic collapse [44]. Hinges form when the localized stress on cell struts is greater than the strut material's compressive yield strength, leading to plastic cellular collapse. Plastic buckling would, then, presumably occur first within those cells most prone to yielding. Combining Eqs. (1) and (3) reveals that low plastic collapse stress results from low

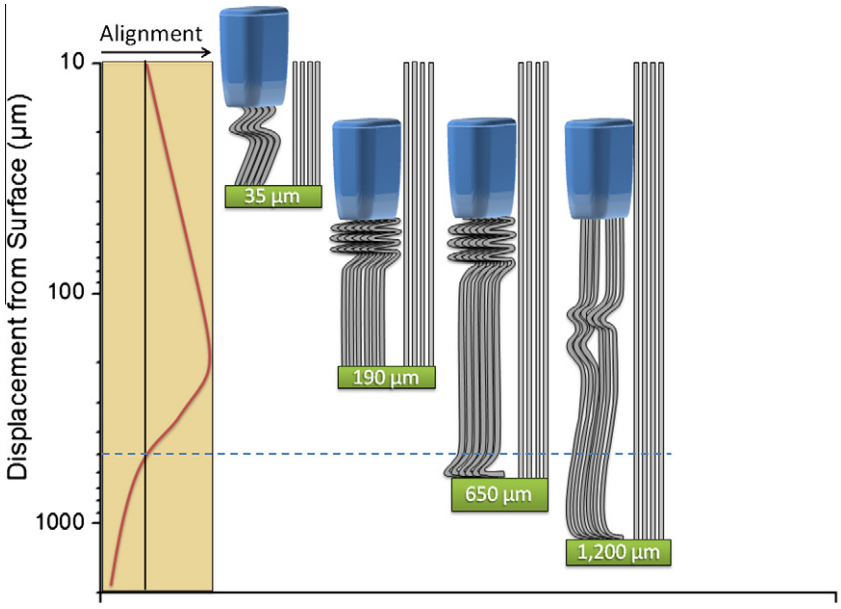

Fig. 7 – Schematic representation of CNT alignment as a function of depth and the resulting compressive buckling formation as a function of array height.

cellular density, which is itself highly sensitive to cellular geometry, as illustrated by the relationship

$$\frac{\sigma_p^*}{\sigma_{ys}} = C_2\left(\frac{t}{l}\right)^3 \quad (4)$$

Assuming consistent cellular shape, Eq. (4) suggest that cells having a broad span perpendicular to axial growth direction (corresponding to low density and perpendicular alignment) would exhibit the lowest yield stress. To that end, Bedewy et al. [45] recently spatially resolved the vertical alignment of CNTs within arrays utilizing synchrotron X-ray scattering. Based on their analysis of the Hermans orientation parameter, vertical CNT alignment and density were observed to increase with depth from the top surface of arrays until an inflection point at a depth of a few hundred micrometers was reached, at which point alignment decreased monotonically with depth. The density and vertical alignment at approximately 500 μm depth had reduced sufficiently to be equivalent to that observed on the surface, and decreased further with depth beyond 500 μm, reaching a minima near the growth substrate. CNT arrays whose growth was terminated prior to attaining 500 μm height exhibited a similar Hermans orientation parameter profile, featuring a maxima near 200 μm of depth and minima near the top surface. Translating these results to the CNT arrays studied herein, we may deduce that cellular elongation and density (and related plastic collapse stress) is lowest at the top surface for all arrays other than the 650 and 1200 μm arrays, where the minima resides near the bottom surface. Raman spectroscopy analysis has likewise revealed that structural defects in super-long CNT arrays, similar in structure to the 1200 μm array, increase as a function of distance from the array top surface. Arguments based upon cellular alignment are also consistent with the buckling behavior observed for liberated arrays, which buckle solely on the bottom surface. As illustrated in Fig. 7, localization of coordinated buckling near the top surface for arrays of moderate heights and additional buckling near the substrate of the 650 and 1200 μm arrays may be explained due to these factors.

3.2. *Lateral force measurement*

Lateral force measurement may provide additional insight both into the magnitude and relative direction of cellular collapse during the buckling events. Fig. 8 shows representative lateral and normal force data obtained from the 650 to 1200 μm arrays. Lateral force oscillations arise at a strain consistent with the onset of normal force oscillations, indicating lateral motion is generated during buckle formation. Although the absolute value of the lateral forces is about an order of magnitude less than that of the normal force during buckling events, the relative change in lateral forces during buckle formation is similar to the changes in compressive force. In fact, a lateral force of up to 10 mN was observed during the rapid onset of buckling for the 1200 μm array. Additionally, forces in the *x*- and *y*-orientations may change from in phase to out of phase relative to each other, consistent with a change in physical orientation of CNTs within collapsed cells. SEM examination of the orientation of CNTs within the buckling folds often reveals a preferential shift in lateral direction that is inconsistent with the orientation of the CNTs outside of the indentation region (see inset of Fig. 6a). The localized CNT orientation between buckles may change by as much as 90° from buckle to buckle. The contribution of lateral forces has not yet been explored relative to CNT buckling mechanics. However, based upon the magnitude of these forces, the lateral contribution to the CNT buckling and folding should not be overlooked and may provide additional evidence of cellular collapse consistent with open-cell foam behavior.

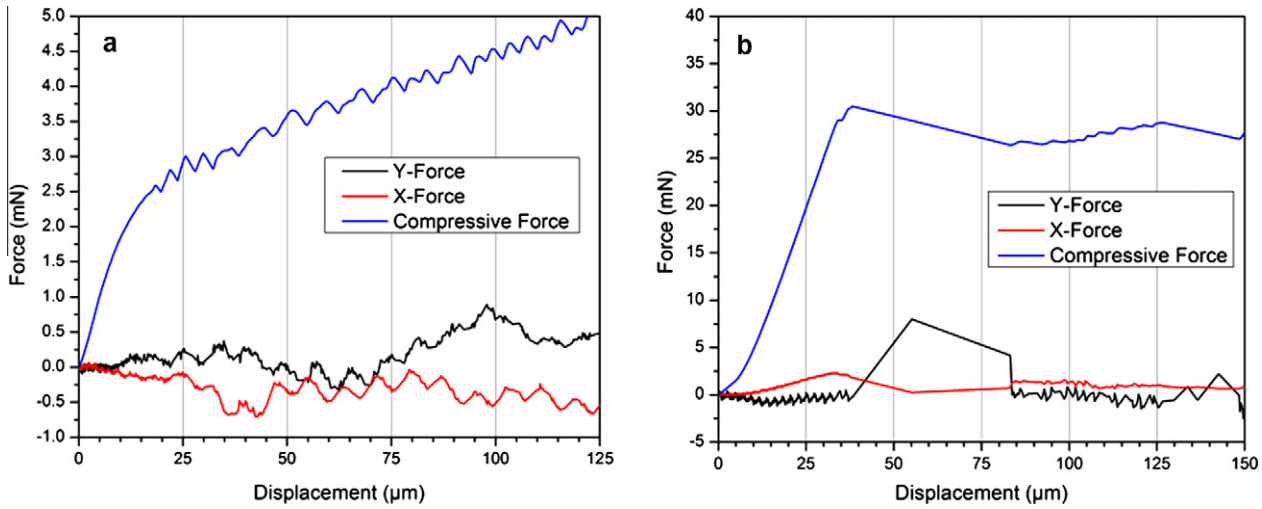

Fig. 8 – Lateral and normal forces measured from (a) 650 μm and (b) 1200 μm CNT array.

3.3. *Compressive elastic modulus*

The compressive elastic modulus of the CNT arrays along the axial direction was evaluated using the CSM technique simultaneously with force–displacement data. The modulus values reported consider full contact between the indenter tip and the CNT arrays and do not account for the variation in volume fraction of CNTs or the potential increase in contact area between the CNTs as the indenter tip load is increased. These assumptions are not strictly accurate, as the arrays are clearly not continuous materials but are, rather, composed of individual CNTs having some occupation fraction much less than unity. Additionally, the free tips of the array likely conform to the indenter face at greater loads, increasing real surface area contact. Nevertheless, the assumption simplifies the computation of material properties and allows for straightforward comparison of results, particularly in the absence of knowing the evolution of real contact area as a function of applied load. The sample elastic modulus was then computed using the following relations for a flat punch indenter:

$$S = \frac{\Delta P}{\Delta h} \tag{5}$$

$$E_r = \frac{\sqrt{\pi}}{2}\frac{S}{\sqrt{A}} \tag{6}$$

$$\frac{1}{E_r} = \frac{(1-\gamma_s^2)}{E_s} + \frac{(1-\gamma_i^2)}{E_i} \tag{7}$$

where S is the unloading stiffness evaluated at 40% unloading, ΔP and Δh are the changes in applied load and displacement from maximum load to 40% unloading, respectively, E is elastic compressive modulus, A is cross-sectional area of the indenter, γ is Poisson's ratio, and the subscripts r, s, and i refer to reduced, sample, and indenter, respectively. The reduced modulus is that which is directly calculated by unloading stiffness during indentation. Poisson's ratio is a very small quantity for CNT arrays and assumed to be zero for computation, as is a common assumption [28,34] and is consistent with our experimental observations.

Fig. 9a and b illustrate the average compressive elastic modulus for each array as a function of both strain and raw indentation depth, respectively. Test-to-test variation in modulus values for a given array was low and similar in magnitude to

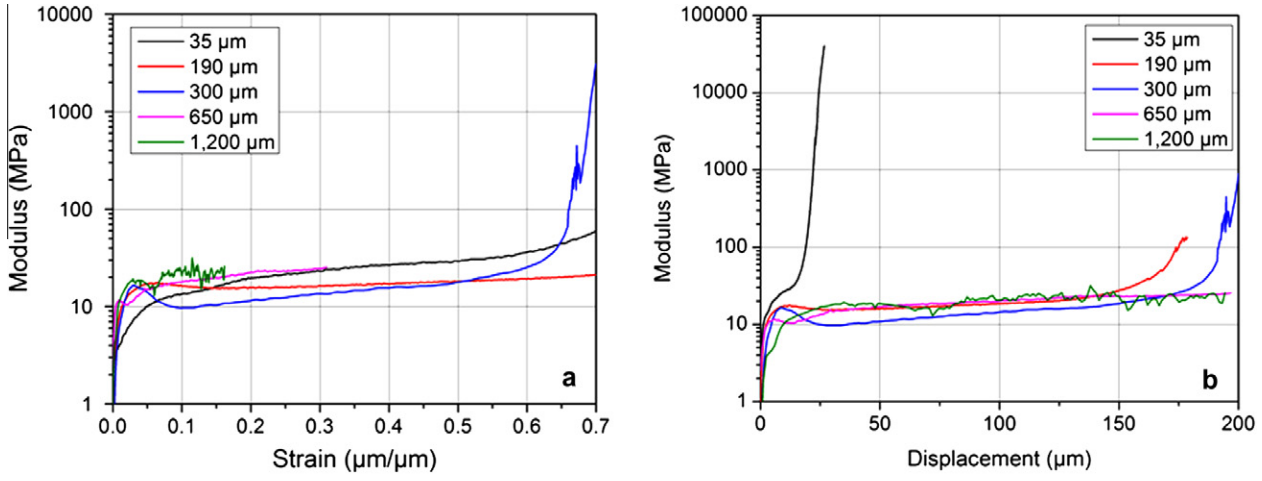

Fig. 9 – Average elastic modulus of CNT arrays as a function of (a) strain and (b) raw displacement.

the noise range of the measurement for these particular materials. Near the surface of the CNT arrays, the elastic modulus monotonically increased as contact was established between the tip and asperities. Because of the inherent nonuniformity of the CNT array height at the free surface due to asperities, the initial area in contact with the indenter face was likely lower than that experienced upon further penetration into the array. Thus, the reported modulus is likely a conservative representation for the initial contact region. The modulus continuously increased with strain to a point approximately corresponding with the yield plateau of the stress–strain profile. The modulus then slowly increased with depth until the densification point, wherein the modulus rapidly increased. Each of the arrays in this investigation exhibited a compressive modulus value between 10 and 20 MPa at the initiation of yield. Remarkably, the magnitude and evolution of elastic compressive modulus as a function of strain is quite similar for all CNT array heights. Because the deformation is largely plastic in nature, the consistent modulus values may be a result of elastic recovery of the top-most asperities, which appear relatively unaffected by indentation, or from elastic recovery of CNTs beneath the buckling region.

4. Conclusions

The axial compressive mechanical behavior of CNT arrays with heights spanning more than an order of magnitude was examined to significant strains using flat punch nanoindentation. It was found that the compressive mechanical response of the CNT arrays behaved similarly to that of open-cell foam of various densities. All arrays exhibited initialization of yielding behavior within a strain of 0.3–0.12, depending upon the array height. Well organized collective buckling was reported for the first time originating from the top surface of CNT arrays, with an additional isolated buckle near the substrate surface observed for arrays obtaining heights of 650 and 1200 μm. This localized buckling was explained in terms of the local cellular geometry variation as a function of depth and compaction of cellular geometries within the arrays. Lateral forces were measured for the first time during CNT buckle formation and indicate a significant lateral component of buckling, providing additional information regarding the cellular collapse mechanisms. The magnitude and relative evolution of the elastic compressive modulus as a function of strain were found to be nearly independent of CNT array height. These results provide significant new insights into CNT array mechanical properties and foam-like behavior as a function of array height.

Acknowledgements

The authors wish to gratefully acknowledge the Air Force Office of Scientific Research (AFOSR), Dr. Byung-Lip (Les) Lee, Program Manager. We would also like to thank Jennifer Hay (Agilent Technologies) for assistance with nanoindentation test method modification, Dr. Matthew O'Malley (AFRL) for TEM analysis and Dr. Rahul Rao (AFRL) for assistance with obtaining Raman spectra.

Appendix A. Supplementary data

Supplementary data associated with this article can be found, in the online version, at doi:10.1016/j.carbon.2010.09.034.

REFERENCES

[1] Xu J, Fisher TS. Enhancement of thermal interface materials with carbon nanotube arrays. Int J Heat Mass Transfer 2006;49(9–10):1658–66.
[2] Panzer MA, Zhang G, Mann D, Hu X, Pop E, Dai H, et al. Thermal properties of metal-coated vertically aligned single-wall nanotube arrays. J Heat Transfer 2008;130(5):052401-1–9.
[3] Cola B, Xu J, Cheng C, Xu X, Fisher T, Hu H. Photoacoustic characterization of carbon nanotube array thermal interfaces. J Appl Phys 2007;101(5):054313-1–9.
[4] Cola BA, Xu J, Fisher TS. Contact mechanics and thermal conductance of carbon nanotube array interfaces. Int J Heat Mass Transfer 2009;52(15–16):3490–503.
[5] Cola B, Xu X, Fisher T. Increased real contact in thermal interfaces: a carbon nanotube/foil material. Appl Phys Lett 2007;90(9):093513-1–3.
[6] Amama P, Cola B, Sands T, Xu X, Fisher T. Dendrimer-assisted controlled growth of carbon nanotubes for enhanced thermal interface conductance. Nanotechnology 2007;18(38):385303.
[7] Sihn S, Ganguli S, Roy AK, Qu L, Dai L. Enhancement of through-thickness thermal conductivity in adhesively bonded joints using aligned carbon nanotubes. Compos Sci Technol 2008;68(3–4):658–65.
[8] Park M, Cola BA, Siegmund T, Xu J, Maschmann MR, Fisher TS, et al. Effects of a carbon nanotube layer on electrical contact resistance between copper substrates. Nanotechnology 2006;17(9):2294–303.
[9] Amama P, Lan C, Cola B, Xu X, Reifenberger R, Fisher T. Electrical and thermal interface conductance of carbon nanotubes grown under direct current bias voltage. J Phys Chem C 2008;112(49):19727–33.
[10] Yaglioglu O, Hart J, Martens R, Slocum A. Method of characterizing electrical contact properties of carbon nanotube coated surfaces. Rev Sci Instrum 2006;77(9):095105-1–3.
[11] Allaoui A, Hoa S, Evesque P, Bai J. Electronic transport in carbon nanotube tangles under compression: the role of contact resistance. Scr Mater 2009;61(6):628–31.
[12] Li J, Ye Q, Cassell A, Ng H, Stevens R, Han J, et al. Bottom-up approach for carbon nanotube interconnects. Appl Phys Lett 2003;82(15):2491–3.
[13] Kreupl F. Carbon nanotubes in interconnect applications. Microelectron Eng 2002;64(1–4):399–408.
[14] Xu T, Miao J, Li H, Wang Z. Local synthesis of aligned carbon nanotube bundle arrays by using integrated micro-heaters for interconnect applications. Nanotechnology 2009;20(29):295303-1–6.
[15] Ci L, Suhr J, Pushparaj V, Zhang X, Ajayan PM. Continuous carbon nanotube reinforced composites. Nano Lett 2008;8(9):2762–6.
[16] Zhang S, Zhu L, Wong C-P, Kumar S. Polymer-infiltrated aligned carbon nanotube fibers by in situ polymerization. Macromol Rapid Commun 2009;30(22):1936–9.
[17] Ma W, Liu L, Zhang Z, Yang R, Liu G, Zhang T, et al. High-strength composite fibers: realizing true potential of carbon nanotubes in polymer matrix through continuous reticulate architecture and molecular level couplings. Nano Lett 2009;9(8):2855–61.
[18] Treacy MMJ, Ebbesen TW, Gibson JM. Exceptionally high Young's modulus observed for individual carbon nanotubes. Nature 1996;381(6584):678–80.

[19] Yu M-F, Lourie O, Dyer M, Moloni K, Kelly T, Ruoff R. Strength and breaking mechanism of multiwalled carbon nanotubes under tensile load. Science 2000;287(5453):637–40.
[20] Ruoff RS, Tersoff J, Lorents DC, Subramoney S, Chan B. Radial deformation of carbon nanotubes by van der Waals forces. Nature 1993;364(6437):514–6.
[21] Gere JM, Timoshenko SP. Mechanics of materials. PWS Publishing; 1997. p. 731–804.
[22] Oliver WC, Pharr GM. An improved technique for determining hardness and elastic modulus using load and displacement sensing indentation experiments. J Mater Res 1992;7:1564–83.
[23] Hay JL, Pharr GM. Instrumented indentation testing. ASM handbook: ASM international; 2000. p. 232–43.
[24] Hay J. Introduction to instrumented indentation testing. Exp Tech 2009;33(6):66–72.
[25] Fischer-Cripps AC. Nanoindentation. New York: Springer-Verlag; 2004. p. 21–66.
[26] Waters JF, Riester L, Jouzi M, Guduru PR, Xu JM. Buckling instabilities in multiwalled carbon nanotubes under uniaxial compression. Appl Phys Lett 2004;85(10):1787–9.
[27] Waters JF, Guduru PR, Xu JM. Nanotube mechanics – recent progress in shell buckling mechanics and quantum electromechanical coupling. Compos Sci Technol 2006;66(9):1141–50.
[28] Zbib AA, Mesarovic D, Lilleodden ET, McClain D, Jiao J, Bahr DF. The coordinated buckling of carbon nanotube turfs under uniform compression. Nanotechnology 2008;19(17):175704-1–7.
[29] Deck CP, Flowers J, McKee GSB, Vecchio K. Mechanical behavior of ultralong multiwalled carbon nanotube mats. J Appl Phys 2007;101(2):23512-1–9.
[30] Tong T, Zhao Y, Delzeit L, Kashani A, Meyyappan M, Majumdar A. Height independent compressive modulus of vertically aligned carbon nanotube arrays. Nano Lett 2008;8(2):511–5.
[31] Misra A, Greer J, Daraio C. Strain rate effects in the mechanical response of polymer-anchored carbon nanotube foams. Adv Mater 2009;21(3):334–8.
[32] Qi HJ, Teo KBK, Lau KKS, Boyce MC, Milne WI, Robertson J, et al. Determination of mechanical properties of carbon nanotubes and vertically aligned carbon nanotube forests using nanoindentation. J Mech Phys Solids 2003;12:2213–37 [UK: Elsevier].
[33] Mesarovic SDj, McCarter CM, Bahr DF, Radhakrishnan H, Richards RF, Richards CD, et al. Mechanical behavior of a carbon nanotube turf. Scr Mater 2007;56(2):157–60.
[34] Pathak S, Cambaz G, Kalidindi S, Swadener G, Gogotsi Y. Viscoelasticity and high buckling stress of dense carbon nanotube brushes. Carbon 2009;47(8):1969–76.
[35] Cao A, Dickrell PL, Sawyer WG, Ghasemi-Nejhad MN, Ajayan PM. Super-compressible foamlike carbon nanotube films. Science 2005;310(5752):1307–13.
[36] Suhr J, Victor P, Ci L, Sreekala S, Zhang X, Nalamasu O, et al. Fatigue resistance of aligned carbon nanotube arrays under cyclic compression. Nat Nanotechnol 2007;2(7):417–21.
[37] Pushparaj VL, Ci L, Sreekala S, Kumar A, Kesapragada S, Gall D, et al. Effects of compressive strains on electrical conductivities of a macroscale carbon nanotube block. Appl Phys Lett 2007;91(15):153116-1–3.
[38] Whitby RLD, Mikhalovsky SV, Gun'ko VM. Mechanical performance of highly compressible multi-walled carbon nanotube columns with hyperboloid geometries. Carbon 2010;48(1):145–52.
[39] Chakrabarti S, Gong K, Dai L. Structural evaluation along the nanotube length for super-long vertically aligned double-walled carbon nanotube arrays. J Phys Chem C 2008;112(22):8136–9.
[40] Hata K, Futaba D, Mizuno K, Namai T, Yumura M, Iijima S. Water-assisted highly efficient synthesis of impurity-free single-walled carbon nanotubes. Science 2004;306(5700):1362–4.
[41] Qu L, Dai L, Stone M, Xia Z, Wang Z. Carbon nanotube arrays with strong shear binding-on and easy normal lifting-off. Science 2008;322(5899):238–42.
[42] Lucas BN, Oliver WC, Pharr GM, Loubet JL. Time dependent deformation during indentation testing. In: Materials research society symposium. San Francisco, CA, USA; 1996. p. 233–8.
[43] Patton ST, Zhang QH, Qu LT, Dai LM, Voevodin AA, Baur J. Electromechanical characterization of carbon nanotubes grown on carbon fiber. J Appl Phys 2009;106(10):104313-1–9 [November].
[44] Gibson LJ, Ashby MF. Cellular solids: structure and properties. Cambridge, United Kingdom: Cambridge University Press; 1997.
[45] Bedewy M, Meshot E, Guo H, Verploegen E, Lu W, Hart J. Collective mechanism for the evolution and self-termination of vertically aligned carbon nanotube growth. J Phys Chem C 2009;113(48):20576–82.